Wavelength-Independent Performance of Femtosecond Laser Dielectric Ablation Spanning Over Three Octaves

Mario Garcia-Lechuga,[1,2,*] Olivier Utéza,[1] Nicolas Sanner,[1] and David Grojo[1,†]

[1] *Aix Marseille Université, CNRS, LP3, UMR7341, 13288 Marseille, France*

[2] *Instituto de Optica Daza de Valdes (IO), CSIC, Serrano 121, 28006 Madrid, Spain*

(Received 21 December 2022; revised 2 March 2023; accepted 14 March 2023; published 18 April 2023)

Ultrafast laser breakdown of wide-band-gap dielectrics is today a key for major technologies ranging from three-dimensional material processing in optical materials to nanosurgery. However, a contradiction persists between the strongly nonlinear character of energy absorption and the robustness of processes to the changes of the band gap:wavelength ratio depending on applications. While various materials and band gaps have been studied, we concentrate here on the investigations of the spectral domain with experiments performed with wavelength drivers varied from deep ultraviolet (258 nm) to midinfrared (3.5 μm). The measured fluence thresholds for single-shot ablation in dielectrics using 200-fs pulses exhibit a plateau extending from the visible domain up to 3.5-μm wavelength. This is accompanied, after ablation crater analysis, by a remarkable invariance of the observed ablation precision and efficiency. Only at the shortest tested wavelength of 258 nm, a twofold decrease of the ablation threshold and significant changes of the machining depths are detected. This defines a lower spectral limit of the wavelength-independence of the ablation process. By comparison with simulations, avalanche ionization coefficients are extracted and compared with those predicted with the Drude model. This must be beneficial to improve predictive models and process engineering developments exploiting the emerging high-power ultrafast laser technologies emitting in various spectral domains.

DOI: 10.1103/PhysRevApplied.19.044047

I. INTRODUCTION

A unique feature with the use of tightly focused ultrashort laser pulses is the ability to achieve localized energy deposition, down to the submicrometer scale at the surface or in the bulk of any materials, even those that are initially transparent to the laser wavelength [1]. This makes femtosecond (fs) lasers a key tool for inducing and controlling transformations of various materials with applications ranging from ultraprecision fabrication of fluidic or optic microdevices [2,3], nanosurgery [4] to warm dense matter physics [5].

Over decades, the efforts on both experimental and theoretical researches [6] have allowed a general picture of ultrafast laser dielectric excitation to be drawn and the resulting potentially extreme conditions to be accessible inside the matter. As reviewed in detail by Balling and Schou [7], and briefly summarized here, the process is triggered by the generation of free carriers induced by strong-field nonlinear ionization (SFI) mechanisms, as multiphoton (MPI) and tunneling ionization (TI), and subsequently increased by impact ionization (IMP). If the excitation is high enough, the transferred energy from the free-electron subsystem to the lattice induces high local temperature and pressure conditions, responsible for material transformations. If the irradiation is performed at the surface, material expansion and ablation can occur [8,9]. This is the basis of industrial micromachining [10] process solutions or high-precision surgery applications [4,11].

The interest on this flexible technology is today accompanied by the advent of alternative source technologies, opening an enormous palette of accessible parameters, such as pulse duration, repetition rate, or wavelength, that are all supposed to influence the strongly nonlinear material responses and so the experimental outcomes. Therefore, the influence of each parameter remains a question of topical interest for fundamental and industrial perspectives.

On one hand, the role of the repetition rate and pulse duration has been widely explored. For example, studies focusing on repetition-rate influence have found benefits on the optimization of waveguide writing at MHz repetition rates [12] and ablation efficiency and cleanliness by using ultrafast pulse trains at GHz repetition rate [13]. Experiments focusing on the pulse duration have revealed that conventional longer femtosecond pulses (>100 fs) leads to significant IMP contributions responsible for

*mario.garcia.lechuga@csic.es
†david.grojo@univ-amu.fr

 © 2023 American Physical Society

plasma absorption assisting laser energy deposition [14–16], whereas energy deposition with the shortest pulses takes more profit from MPI [17,18] and even TI when few-cycle pulses are applied [19,20].

On the other hand, the wavelength has been the subject of less investigations. Most probably this is because the fundamental wavelength of most available ultrafast laser technologies remained confined until recently in a relatively narrow spectral domain in the near infrared (typically 800 nm or 1.03 μm for, respectively, Ti:sapphire or Yb-doped-crystal technologies). With the recently available compact technologies delivering increased power in alternative spectral regions and, in particular, the midinfrared domain (including fiber technologies), one should reasonably expect the possibility to cause drastic changes in the balance between the above-described physical processes. By affecting the relative role of MPI, TI, and IMP, one can look for optimization on the drivers for energy deposition. This introduces the timeliness for a debate of the achievable performance for precision processing considering the full spectrum covered with the alternatively available sources.

From a fundamental perspective, one can refer to the Keldysh theories that directly account for the wavelength dependence of nonlinear ionization [21,22]. For the experimental works (including ours), one usually relies on studies with optical parametric amplifiers (OPAs). These become routinely available in laboratories and allow a continuous tuning of radiations for assessing the detailed spectral dependencies of material responses.

The number of works on this subject remains scarce but it is worthwhile to refer to the pioneering works of Simanovskii *et al*. [23] and Jia *et al*. [24], measuring the breakdown fluence thresholds at the surface of several dielectrics with varying wavelength conditions. Despite the gap separating the spectral domains, which were investigated in these two works, one can already extrapolate from their combination a relative invariance of the apparent nonlinear absorption rates (within experimental uncertainty) in a broad spectral region. It is only at the tested spectral limits that a significant change could be observed. In their study concentrating in the midinfrared, Simanovskii *et al*. [23] measured a drop for the breakdown threshold fluence when increasing the wavelength above 5 μm. According to the electronic transition picture described above, this was attributed to a breakdown process that becomes seeded by TI, a wavelength-independent process [25] but driven by IMP with efficiency scaling with the wavelength according to a simple Drude model. However, the investigated spectral domain up to 7.8 μm is at the edge of the vibrational absorption bands, an aspect that raises question on an interpretation solely based on the ionization yield. A similar increase of absorption efficiency is also reported approaching the UV part of the spectrum by Jia *et al*. [24]. While this can be directly interpreted by increased ionization rates with a pure MPI picture, the authors had also to introduce significant contributions from sub-conduction-band transitions to quantitatively describe the measured process efficiency at short wavelengths.

It is only recently that more experimental investigations have been added on these questions. Gallais and coauthors [26] measured femtosecond laser induced damage thresholds of various band-gap materials (1 to 10 eV) in a spectral region from 310 to 1030 nm. While the paper was concentrating on thin-film materials, the measured thresholds for silica substrates and the reported wavelength dependence compares reasonably well with Jia *et al*. [24]. For recent investigations turned toward the midinfrared part of the spectrum, one can turn to Migal *et al.* [27] who investigated the breakdown response of SiO_2 and MgF_2. The reported thresholds were strongly deviating from those in the pioneering paper of Simanovskii *et al.* [23]. However, this and another work conducted by Austin *et al*. [28] on narrow-gap material as germanium concluded that the conventional nonlinear ionization models fail in describing the midinfrared response. Multiband and/or intra-conduction-band effects are then considered to discuss the obtained results.

Among the other related works, the laser wavelength influence has been studied on the direct writing of optical waveguides or other buried structures in glasses [29] and in silicon [30]. Additionally for a silicon surface, we reported the optimization of amorphization by tuning the laser wavelength (258 nm to 4 μm) [31] and Otobe theoretically studied the wavelength dependence (800 nm to 3 μm) of laser excitation [32]. We can also mention the study of laser-induced breakdown in water [33] or on ablation of corneal stroma [11]. While all are relevant for fundamental and technological considerations, the results obtained in these specific configurations are more hardly comparable to the previously mentioned papers focused on material dielectric ablation.

In this paper, we bridge the gap between these previous reports by investigating the femtosecond laser ablation response in an unprecedented spectral range from 258 to 3500 nm. We find nearly invariant observables including ablation fluence thresholds, thermally affected zones or maximum crater depths on a very large spectral domain from the visible to the midinfrared part of the spectrum. Supported by simulations, we concentrate the analyses on sapphire and fused silica, dielectric materials of reference both in applications and in the fundamental study of laser-matter interaction. Simple nonlinear absorption rate considerations lead to the report of apparent avalanche rates, which are compared with those that can be derived by a Drude model. The gained knowledge on the spectral dependence of femtosecond laser machining is discussed in terms of potential optimizations in model and application developments.

II. METHODS

A. Laser system and optical setup

The multiwavelength study is performed by using a commercial femtosecond amplifier (Pharos, Light Conversion) emitting at 1030 nm with pulse energies up to 500-μJ and 180 ± 10-fs pulse duration at FWHM, characterized by single-shot autocorrelation (TiPA, Light Conversion). Tunable near-infrared (NIR) and midinfrared (MIR) radiation is accessible through optical parametric amplification (Orpheus, Light Conversion), designed for efficient conversion on a large infrared range (signal, 1.5 μm−2.06 μm; idler, 2.06–5 μm). In this work, we perform experiments up to 3.5 μm (MIR), due to the limited pulse energy on longer wavelengths. Indeed, the use of tight focusing conditions is avoided in order to maintain the same *ex situ* characterization methodology (as explained later on) for all the analyses. Visible (VIS) and ultraviolet (UV) radiation (515 and 258 nm) are obtained through harmonic generation (Hiro, Light Conversion). For all the wavelengths, the beam irradiates the targets at normal incidence with linear polarization.

Using the already mentioned autocorrelator device, we measure pulse durations of 190 ± 10 fs FWHM on the range from 1.55 μm to 2 μm and 160 ± 10-fs FWHM at 515 nm. Temporal characterization on the idler spectral range could not be performed with the employed instrument. However, a direct correspondence of the pulse duration is expected between signal and idler, given the optical parametric amplification process generating both beams together. For the deep ultraviolet, we also expect a pulse duration very close to the one measured at 515 nm according to the design (thickness) of the last doubling crystal for generating the 258-nm radiation.

A sketch of the experimental setup is shown in Fig. 1. Experiments are performed on the basis of single-shot irradiations, by making use of a pulse picker at the output of the femtosecond amplifier. For each selected wavelength, the beam is directed toward the same irradiation beam line. Gold mirrors are used for the beams in the midinfrared domain covered by the OPA. For the other beams, these are systematically replaced by specific high-reflectivity dielectric mirrors to reduce energy losses and assure excellent spectral filtering at the considered wavelength. The selected beam is then focused normally onto the sample surface by means of an uncoated UV-fused silica aspheric lens (nominal $f = 50$ mm) for the spectral range between 248 nm to 2 μm, and a calcium fluoride planoconvex lens (nominal $f = 25$ mm) from 2.2 to 3.5 μm. These choices of materials and focal distances are made because of two reasons: the loss of transparency of UV-fused silica in the infrared range and the reduction of accessible energy in the infrared range. A ring-actuated iris diaphragm is situated as close as possible to the lens to truncate all beams (transmitted power approximately 75%) and so we always irradiate the samples with well-defined profiles. This is of relevance to suppress potential biases in the analyses caused by some of the OPA beam profiles exhibiting pedestals [34].

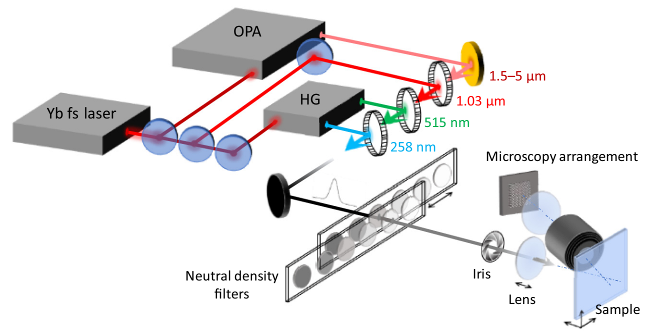

FIG. 1. Sketch of the experimental setup. The top part represents the beams of different wavelengths obtained from the same master femtosecond laser through harmonic generation (HG), for ultraviolet and visible radiation, and optical parametric amplification (OPA), for infrared radiation. On the bottom part, the main optical elements of the irradiation configuration are represented including an *in situ* microscopy system for precise positioning of the focal spot on the surface. The OPA beams are directed toward the irradiation setup using gold mirrors. A selection of dielectric mirrors is used for the other wavelengths (removable mirrors shown by empty volumes).

On the beam path, a motorized wheel with neutral density metallic filters (1-mm UV-fused silica substrate with nickel coating) is placed. The broadband response of the filters allows the pulse energy to be controlled on the full spectral region of interest in this work. For all experiments, the applied power is measured at 1-kHz repetition rate with a thermal powermeter (3A, Ophir), which is calibrated for the spectral range of interest. Peak-to-peak pulse-energy stability is measured by a pyroelectric energy meter (PE9, Ophir) to be less than 4% for all the considered wavelengths, being sufficiently low for making unnecessary a measurement of the energy of each applied pulse. Since the powermeter is placed just before the lens, the energy at the sample position is obtained by simply accounting for the Fresnel reflection losses expected on the lens surfaces.

The sample is mounted on *XYZ* motorized stages and aligned perpendicular to the irradiation axis. Precise parallelism of the sample with respect to motion axes is achieved by using a two-axis kinematic sample holder. Motion in the *XY* plane, perpendicular to the axis of laser incidence, allows the sample to be positioned on a fresh surface before each irradiation. Optimal focusing position is determined empirically by a *Z* scanning procedure and surface imaging with an *in situ* microscopy (10× microscope objective, tube lens, and CCD camera) placed at 45° as shown in Fig. 1. Repositioning of the different samples at the best focal position is guaranteed by exploiting the approximately equal to 10-μm depth of field of the microscopy system.

B. Samples and metrology

In this work we study four different samples of three dielectric materials widely used in optics and photonics applications: sapphire, soda-lime glass, and fused silica (amorphous, a-SiO_2). The sapphire sample is a sapphire window from Meller Optics, Inc. (2 mm thick). The soda-lime glass sample is a microscope slide from Corning (1 mm thick). Two different samples of fused silica are studied. First a sample of synthetic fused silica (Suprasil 2) from Heraeus of 3 mm thickness, being superpolished by Thales-SESO (with measured Ra = 0.2 nm). The same sample is used for some other studies conducted by our group [15]. For this work, it is named as "UV-fused silica." Second is a sample of fused quartz provided by Thuet-France (1 mm thick), named on here as "IR-fused silica." The transmittivity in the ultraviolet region of the spectrum differs on these two samples, being observed by spectrophotometry measurements (UV-2600, Shimadzu, range 190–1500 nm). Measurable absorption is found at 250 nm (approximately 5 eV) for IR-fused silica. In contrast, the full transparency in this UV domain for UV-fused silica is consistent with the expected absorption edge according to the band gaps considered in the literature from 7.75 to 9.9 eV (7.75 eV used by Gallais *et al.* [35], 9.6 eV reported by Ravindra *et al.* [36], 8.9 eV indirect or 9.9 eV direct band gap reported by Tan *et al.* [37]). The same measurements performed for the other samples reveal absorption under approximately 350 nm in soda-lime glass corresponding to an apparent optical band gap of approximately 3.5 eV. The absence of measurable absorption in sapphire for the entire measured spectral range is consistent with the band gap of 8.8 eV from the literature [38].

For characterizing the laser-induced modifications on the different samples, we use confocal microscopy (Leica DCM3D). Under monochromatic illumination (460 nm) and using a 150× objective lens (NA 0.95), the laser-induced modifications are characterized with transverse submicrometer spatial resolution and nanometric vertical resolution. This technique allows characterization of the ablated area on different samples under a removal depth-based criterion suppressing any potential subjectivity in the analyses. This is a major advantage in comparison to methods relying on conventional optical microscopy where the interpretation is based on an apparent optical contrast, which can be dependent on the nature of modifications and material responses. Another advantage of the confocal microscopy method compatible with a well-defined and fixed threshold criterion is the possibility to achieve automated crater analyses using a software-solution (Mountains 8, Digital Surf) as demonstrated in previous works [39,40].

In Fig. 2(a), we show examples of craters produced on each of the mentioned samples, after irradiation by a single pulse at 1.7-μm wavelength. The grayscale of the

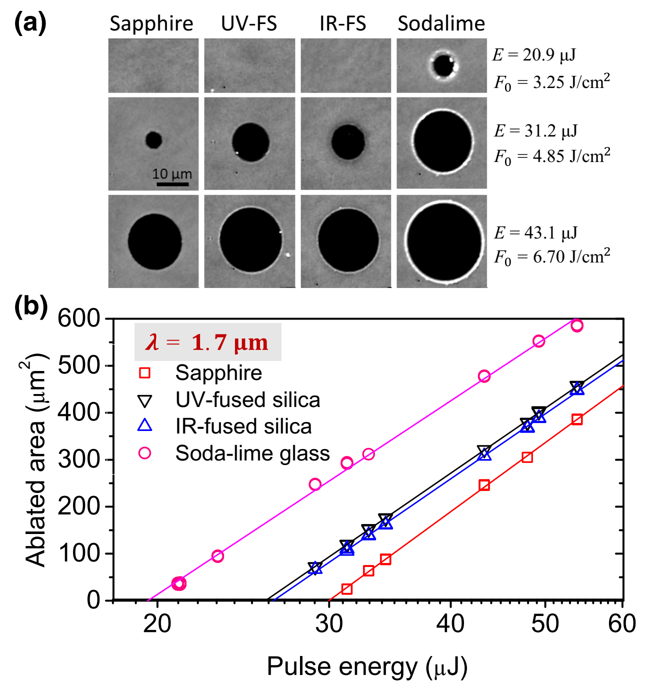

FIG. 2. (a) Confocal microscopy images (profilometry) of craters induced in four different dielectrics with 1700-nm laser pulses of different energies. The grayscale is set so that depressions and elevations are represented, respectively, with darker and brighter tones with respect to the gray background. (b) Ablated area as a function of the pulse energy for four different materials. Lines correspond to numerical linear regressions following Liu's methodology.

images is set to show in black the surface depressions and in white the surface elevations. Subsequent analyses of the images allow the total ablated area (depression region taken under −10-nm level) and the crater profile to be obtained (some examples are shown within the Supplemental Material [41]).

As part also of the metrology, firstly, each irradiation condition (each energy on each material) is repeated three times in order to add statistics to our analysis. Secondly, the fluence threshold in this work is obtained by following Liu's method [42]. However, this is rigorously valid for perfect Gaussian beams. This deviated from some of our OPA beam profiles exhibiting a pedestal (e.g., see the profile at 1.55 μm in Ref. [39]) and it is the reason of the truncation of all our beams by using a circular aperture. In this way, we do not irradiate with Gaussian spots but systematically with well-defined Airy-like beam shapes that allow the calculation for correction factors to the threshold determination. The details corresponding to this applied procedure extending Liu's method to imperfect beams is described and demonstrated in Ref. [34].

In Fig. 2(b) the representation following Liu's methodology is shown, where the ablated area of the craters,

as the ones shown in Fig. 2(a), are represented as a function of the pulse energy (in logarithmic scale). A linear regression enables extraction of an energy threshold (E_{th}) and an equivalent Gaussian beam waist ($w_{0,\text{Liu}}$). The fluence threshold value is then obtained as $F_{\text{th}} = (2E_{\text{th}}/\pi w_{0,\text{Liu}}^2)\eta_{E_{\text{th}}}\eta_F$, with $\eta_{E_{\text{th}}}$ and η_F the correction factors to apply for a truncated beam (Airy-like beam on target) [34]. Rigorously, those correction factors depend on the power transfer of the aperture (P_T) and the maximum excitation energy considered for the linear fitting procedure (ME) [34]. P_T, ME, and values of the retrieved $w_{0,\text{Liu}}$ can be found within the Supplemental Material [41].

C. Modeling

For evaluation of the relative roles of the ionization mechanisms depending on tested radiations, we perform calculations of the temporal evolution of the electron density on the conduction band, $n_e(t)$ according to the standard electron-density single-rate equation:

$$\frac{dn_e(t)}{dt} = \frac{n_T - n_e}{n_T}(W_{\text{SFI}}(I(t)) + \alpha \times I(t) \times n_e(t)), \quad (1)$$

where n_T is the total density of accessible electrons (valence electron density) in the medium as described by Christensen and Balling [43] and fixed at $n_T = 1 \times 10^{23}$ cm^{-3}. The first term, W_{SFI}, is the photoionization rate by SFI (MPI or/and TI) and the second term represents the contribution of IMP, where α is the avalanche coefficient and $I(t)$ is the instantaneous laser intensity. For simplification, here we neglect all the relaxation sources (including electron trapping mechanisms).

The term W_{SFI} is calculated from the Keldysh formalism [21], dependent on the conditions of irradiation (laser intensity and wavelength) and on the material properties (material band gap). In this work, we perform calculations for sapphire and UV-fused silica assuming band gaps of 8.8 [38] and 8.9 eV [37], respectively. As an example, Fig. 3(a) shows the calculated W_{SFI} values for sapphire on the range of laser wavelengths and laser intensities investigated in this work. On the same graph, we append several isocontour lines representing the Keldysh adiabatic parameter $\gamma = \omega\sqrt{m^* \times E_{\text{gap}}}/(e \times E)$, ($m^*$, E, and E_{gap} are, respectively, the reduced mass of the electron-hole pair, the laser electric field, and the band gap of the material). The γ-parameter is usually referred to when discussing the relative significance of MPI and TI. When $\gamma \gg 1$ MPI is expected to dominate, corresponding for the calculated example to irradiations in the UV-visible range or when irradiating on the NIR with intensities well under the modest TW cm^{-2} level. When $\gamma \ll 1$ TI dominates, corresponding to extremely strong laser fields or long wavelengths regimes (MIR) with intensities exceeding 10 TW cm^{-2}.

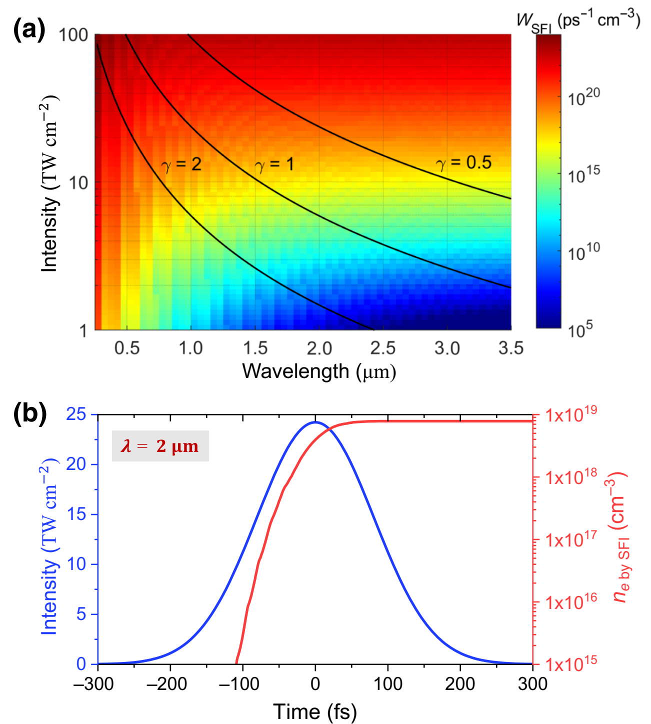

FIG. 3. (a) Numerical calculation of the strong-field photoionization rate (W_{SFI}) as a function of the wavelength and intensity (ranges investigated in this work) following the Keldysh formulation for sapphire (band gap equal to 8.8 eV) and considering $m^* = m_e$. To assess the transition from TI ($\gamma \ll 1$) to MPI ($\gamma \gg 1$), contour lines for given adiabatic coefficients ($\gamma = 2, \gamma = 1, \gamma = 0.5$) are appended. (b) (Blue line) Intensity temporal profile of a pulse of 190 fs (FWHM) for a fluence of 4.9 J cm^{-2} corresponding to the measured fluence threshold for ablation of sapphire at λ = 2 μm. (Red line) Corresponding buildup of the free electron population expected from the strong field ionization (time integral).

An example of application of Eq. (1) when accounting only its first term (only SFI) is shown in Fig. 3(b). Plotted in blue the temporal profile is represented in intensity for a 190-fs pulse. The integration over time leads to a fluence value of 4.9 J cm^{-2}, which, as shown later on, corresponds to the ablation fluence threshold of sapphire at a wavelength of $\lambda = 2$ μm. Additionally, the free electron generation by SFI in sapphire is calculated according to Eq. (1) using these pulse characteristics. Under these conditions, we note that the photoionization channel leads to the creation of a free-electron density with a maximum predicted at around 8×10^{18} cm^{-3}.

The second term on the right side of Eq. (1) accounts for the contribution of IMP. A way to account for a wavelength dependence of this coefficient can be to rely on the semiclassical Drude formalism, where the avalanche coefficient

is expressed as

$$\alpha(\omega) = \frac{\sigma}{E_{\text{gap}}} = \frac{1}{E_{\text{gap}}} \frac{e^2}{n(\omega) \times m^* c\, \epsilon_0} \frac{\tau_c}{1 + \omega^2 \times \tau_c^2}, \quad (2)$$

where σ is the inverse Bremsstrahlung absorption cross section, $n(\omega)$ the refractive index of the irradiated material at the excitation wavelength, c the speed of light, ϵ_0 the vacuum permittivity, and τ_c the free-electron scattering time.

This last term depends on the free-electron density and electron temperature (T_e), being a dynamic parameter during the pulse [44,45]. This dependency on the complex light-matter interaction process makes it hard to derive a robust description of τ_c (n_e, T_e). On the framework of this work, this description would be even harder since a large spectral range and different materials should be accounted for.

An interesting study of Rajeev *et al.* [14] revealed a field dependence of the apparent avalanche coefficient by irradiating dielectrics with different pulse durations. In our work, inspired by this study, we decide to extract from our ablation threshold measurements, apparent avalanche coefficients by fixing an absorbed energy-density target to be reached at the end of the irradiation pulse for ablation. While this approach will not permit description of the detailed aspect of the underlying physics, it leads to the interesting possibility for a phenomenological modeling of the wavelength dependence of femtosecond laser ablation using the usual electron-density rate equation [Eq. (1)].

III. RESULTS AND DISCUSSION

A. Fluence ablation threshold as a function of the wavelength

The measured ablation fluence thresholds as a function of the wavelength are represented in Fig. 4(a) for the four different samples (the values can be found in Appendix A). Determination criteria of ablation fluence threshold, F_{th}, together with its errors, and the equivalent Gaussian beam waist, $w_{0,\text{Liu}}$, can be found within the Supplemental Material [41].

As a first general observation, one can note that despite an exploration over more than five octaves the relative changes of the fluence threshold does not exceed a factor of 3. This and the positions for the minimum (ultraviolet) and the maximum threshold values (near infrared) are common features for all the considered dielectric materials. Concentrating on fused silica, we report on a maximum relative change of only 1.9, marking a significant difference with the study of Jia *et al.* [24] where threshold changes exceeding a factor 3 are reported. While the pulse duration (150-fs pulse duration) and the investigated spectral range (260 nm to 1.7 μm) are comparable, one can however attribute this difference to a material incubation response. We make this comment in regard to our single-shot study in comparison to Jia's work [24] considering the effect of three applied pulses. This is also supported by a more comparable result reported by Gallais *et al.* [26] where a factor of difference of approximately 2.5 was reported for single-pulse irradiations for fused silica (310–1030 nm, pulse duration approximately 100 fs).

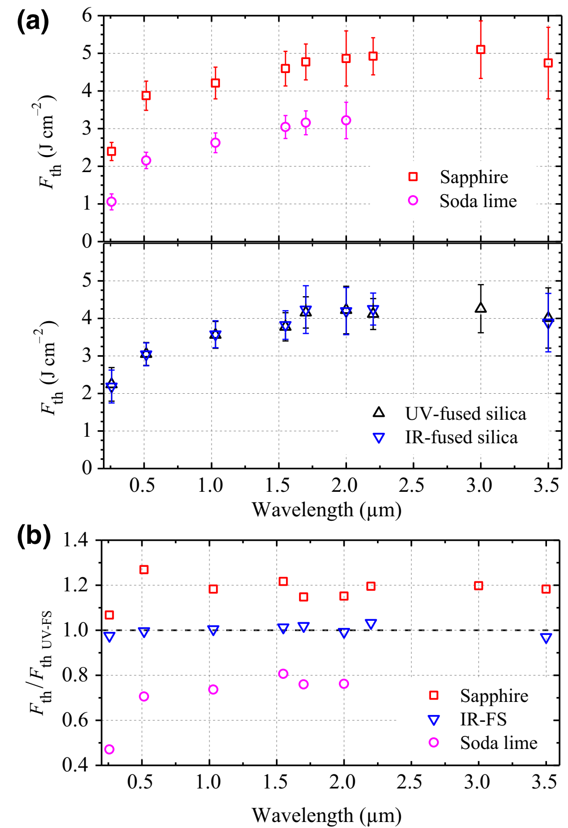

FIG. 4. (a) Single-pulse fluence threshold for femtosecond laser ablation of dielectrics with different wavelengths. (b) Measured ablation fluence thresholds for the different materials normalized to values obtained for UV-fused silica (reference for material comparisons).

A second observed tendency for all materials is a near invariance of the measured thresholds all over the infrared range (from 1.03 to 3.5 μm). After a steep increase on the fluence ablation threshold from the UV to the near infrared (258 to 1030 nm), a very moderate increase on the short-wave infrared regime followed by a stabilization up to 3.5 μm is noted. This result reproduces the observation reported by Jia *et al.* up to 1.7 μm [21] in fused silica and calcium fluoride, and confirms the constancy of the ablation response deeper to the infrared (up to 3.5 μm). For an interpretation of this characteristic response, calculations and discussions about the relative role of the different ionization processes will be pursued in Sec. B.

Looking now in more detail at the material responses, we clearly observe differences between them over all the

spectral range: reaching the highest values for sapphire and the lowest for soda lime. Apart from that, two observations deserve a particular attention.

First, similar values are obtained on the two fused-silica samples. As mentioned on the sample description, the linear optical response of the two samples is different, with absorption observed in the IR-fused silica at wavelengths around 250 nm (approximately 5 eV). This indicates a different optical material band gap, which should be reflected by different nonlinear absorption response and finally different fluence thresholds for modification. Nevertheless, Fig. 4(b) does not confirm this point by showing very similar thresholds found for both materials independently of the wavelength. Accordingly, the discussion on the relative change of the fluence threshold values between materials cannot be reduced to the simple band-gap difference.

Second, the comparison between samples shown in Fig. 4(b), reveals also an almost constant ratio between measured thresholds approximately $\times 1.2$, between fused silica and sapphire. Interestingly, some previous studies irradiating those two materials with different conditions found similar relative differences. Puerto *et al*. [46], (120 fs, 800 nm, and angle of incidence of 53°) reported an ablation fluence threshold of 5.4 J cm^{-2} for fused silica and 7.0 J cm^{-2} for sapphire, that is a relative difference of 1.30. Garcia-Lechuga *et al*. [47] (120 fs, 800 nm) reported fluence thresholds at 3.7 J cm^{-2} for fused silica and 4.6 J cm^{-2} for sapphire. These values and the corresponding difference factor of 1.24 compare remarkably well with our measurements for $\lambda = 1030$ nm. Overall, Fig. 4(b) tends to confirm more the material-dependent differences than a wavelength-dependent response. This holds very well for all studied cases at the exception of the UV domain.

This difference in material responses is again not directly related with the material band gaps (sapphire, 8.8 eV; UV-fused silica, 8.9 eV), leading to a conclusion, which deviates from the one extracted from the work by Gallais and coworkers [26]. Looking at the other material properties that could be associated with the observed differences between the two materials, one can refer to the findings of Grehn and coauthors [48] and compare the ratio difference between the dissociation energies of two materials:

$$\frac{E_{\text{diss}}(\text{Sapp})}{E_{\text{diss}}(\text{FS})} = \frac{78 \text{ kJ cm}^{-3}}{65 \text{ kJ cm}^{-3}} = 1.2. \quad (3)$$

This ratio compares very favorably with the measured fluence thresholds for ablation. Therefore, the dissociation energy could be hypothesized as the parameter of major significance for understanding the relatively modest differences between the fluence threshold for ablation observed between dielectrics. This leads to the hypothesis of nonlinear energy deposition with femtosecond pulses nearly independent of the considered dielectric material (same wavelength dependencies) and of threshold values mainly related to a critical dissociation energy to be reached and depending on materials (constant differences). This second observation appears to hold true when comparing fused silica and sapphire with pulse durations in the range of few hundreds of femtosecond. However, we cannot directly extrapolate this observation to other pulse durations (e.g., Temnov *et al*. [17] by using 800-nm 50-fs pulses report a $\times 1.7$ factor between measured thresholds).

Additional comparisons extended to other materials would also be needed to confirm the generality of this observation. Nevertheless, this view on referring to the dissociation energy can support the observation of identical response for the two fused silica samples. For these two materials, the different linear absorption response is attributed to the material purity level (defect absorption). According to the very deterministic ablation response in the ultrafast regime, it is commonly accepted that the nonlinear ionization response becomes independent to defects because the number of produced carriers during the pulse largely exceeds the material defect densities. Also, we expect the dissociation energy to be a macroscopic material property that will not depend on low-density defects. Overall, the identical ablation thresholds found for these samples is then interpreted as a direct consequence of these retained considerations for our analysis.

B. Relatives roles of ionization processes at fluence threshold levels

From now, we concentrate only on fused silica and sapphire, being two of the most studied and widely used dielectrics for applications. For the particular case of fused silica, modeling considers only the experimental data and band gap of UV-fused silica.

In Fig. 5, we represent the Keldysh adiabatic parameter calculated considering the peak intensity at fluence threshold conditions (values on Fig. 4) for sapphire and fused silica. It can be observed on both cases that values well

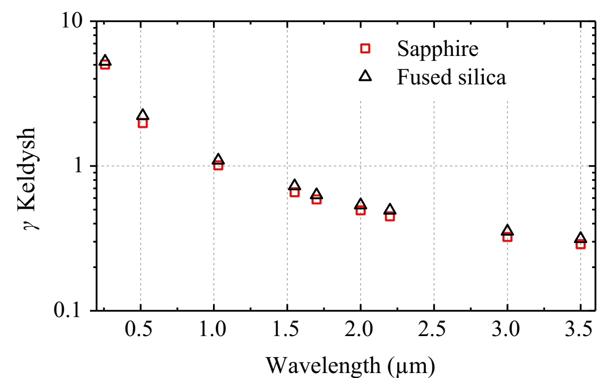

FIG. 5. Calculated Keldysh adiabatic parameter for fused silica and sapphire as a function of the wavelength at peak intensities corresponding to the experimentally obtained fluence threshold of ablation.

above unity are only occurring for 258 and 515 nm. Therefore, only for the UV-VIS spectral region, MPI is expected as the dominant photoionization mechanism. From 1.55-μm wavelength (NIR and MIR radiation) the Keldysh parameter becomes significantly smaller than one, which corresponds to a dominance of TI. It is striking to note that the most commonly studied ablation conditions near 1 μm actually correspond to the apparently most complex situation with a mix between the two processes ($\gamma \sim 1$).

On a first attempt to explain the threshold tendency observed in Fig. 4, we can reasonably attribute the increasing values of fluence threshold for ablation from UV to VIS to an increase on the multiphoton order and so a corresponding decrease of the MPI yield. The near invariant ablation fluence threshold values in NIR and MIR is, respectively, consistent with the expected wavelength-independent response when TI becomes the dominant ionization mechanism [25]. This leads to an overall qualitatively consistent picture but with a validity obviously limited due to an absence of consideration of the collision-assisted ionization processes.

In order to enlarge the information that can be extracted from experimental data, we perform calculations of the free electrons generated by SFI for each experimentally determined threshold condition, as shown as the example in Fig. 3(b). The calculated values of n_e by SFI for fused silica and for sapphire are plotted on Fig. 6(a). Under UV radiation, electron densities generated by SFI exceed 10^{21} cm^{-3}, corresponding to high excitation values above 1% of the total valence electron density ($n_T = 1 \times 10^{23}$ cm^{-3}). However, for VIS, NIR, and MIR regimes, the percentage of generated free electrons by SFI shown in Fig. 6 varies between 0.1% and 0.001% of the valence density. These calculated percentages are far below the physical conditions expected for the occurrence of ablation (e.g., 2% set by Christensen and Balling [43]), and thus directly indicates a largely increasing significance of the impact ionization mechanism (IMP) in energy deposition.

After showing, in Sec. A, a correlation between ablation fluence threshold and dissociation energy in a similar way that it was also stated by Grehn and coauthors [48], we propose in this work a simplified expression to evaluate the level of energy deposition and to establish a direct comparison with the dissociation energy. Ignoring the potential energy stored by acceleration of free electrons in the conduction (absence of hot electrons), we convert the created free-carrier density directly in deposited energy density, E_{dep}, according to

$$E_{\text{dep}}[\text{kJ cm}^{-3}] = E_{\text{gap}}[\text{kJ}] * n_e[\text{cm}^{-3}], \tag{4}$$

with this conversion, we simply consider that each electron promoted from the valence to the conduction band has required the absorption of sufficient energy from the laser pulse to span the material band gap of energy, E_{gap}. Those estimates at threshold conditions for sapphire and fused silica are plotted in Fig. 6(b). The values obtained for the full spectral range are largely below the dissociation energy of the considered materials.

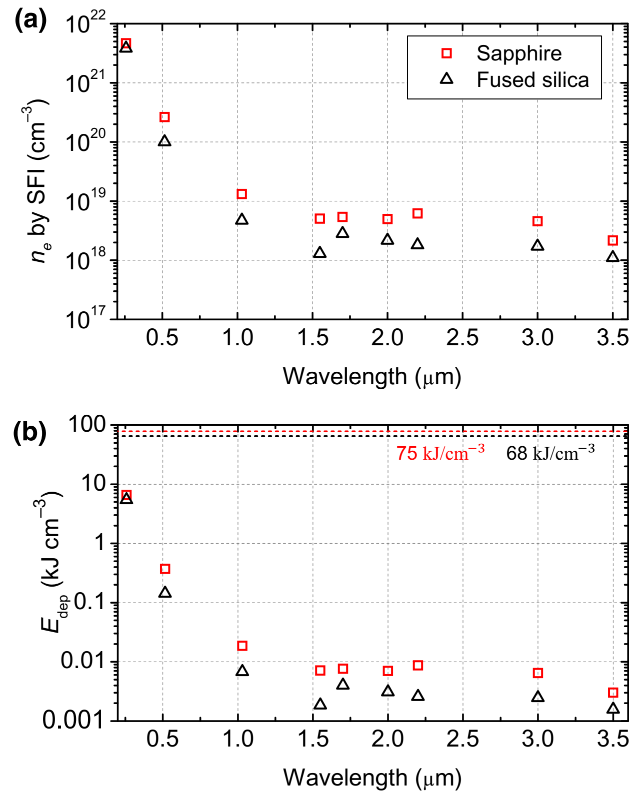

FIG. 6. (a) Numerical calculations of the maximum free-electron density obtained by SFI in UV-fused silica and in sapphire at the fluence threshold level. (b) Estimations of the corresponding minimal deposited energy to create the calculated free-carrier population. Dashed lines represent the dissociation energy of both materials for comparisons.

In order to account for the potential contribution of IMP, we calculate the apparent avalanche coefficient values for each considered wavelength ($\alpha(\lambda)$), so that the deposited energy equals the dissociation energy. In practice, we implement a calculation procedure based on Eqs. (1) and (4), which iteratively tests different avalanche coefficient values until a match is obtained between energy densities. The obtained avalanche coefficients for both materials are plotted in Fig. 7. As shown in the figure, higher values are obtained for fused silica than for sapphire. This is a direct consequence of a deposited energy by SFI, which is less efficient than for sapphire [Fig. 6(b)] while dissociation energies are not differing much. Additionally, both materials show a similar tendency with low variations in NIR-MIR spectral range and an increase of typically a factor 2 from the shortest considered wavelength in UV to the end of the VIS region.

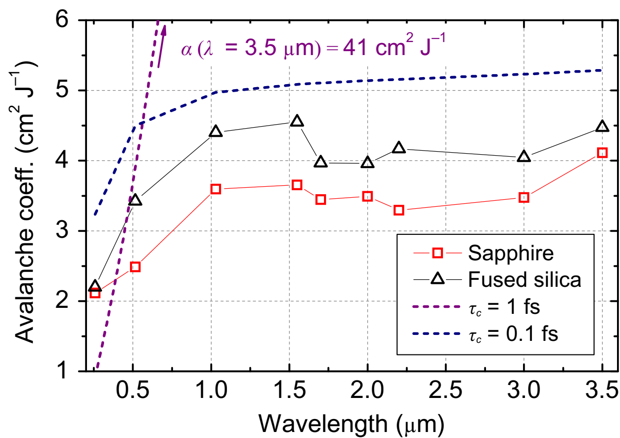

FIG. 7. (Symbols) Estimated wavelength-dependent avalanche coefficients for deposition of an energy density equal to the dissociation energy of the material [Eqs. (1) and (4)] at fluence threshold conditions for ablation (measured). (Dashed lines) Calculated avalanche coefficients following the Drude model [Eq. (2)] for fused silica (considering two different collision rates).

Therefore, observing the tendencies on Figs. 6(a) and 7, we conclude on nearly invariant SFI and IMP contributions in the NIR-MIR for the studied dielectric materials. It is worth noting that this picture differs from the interpretation of Jia and coworkers [24]. A plateau on the ablation fluence threshold in the infrared was also observed in their study but this trend was interpreted based on an increasing significance of IMP compensating an expected decrease of the SFI yield towards the infrared.

As stated before, a simple way to calculate avalanche coefficients without the presented comparison between simulation and measurement results is to use the Drude model [Eq. (2)]. For comparison, we present in Fig. 7 (dashed lines) calculations taking the electron mass for m^*, the physical properties of fused silica (band gap and refractive index [49]) and two different values for the carrier scattering time ($\tau_c = 1$ fs and $\tau_c = 0.1$ fs). In comparison to our analysis, the Drude model calculations with $\tau_c = 1$ fs lead to values that underestimate the contribution of IMP in the UV and strongly overestimate it at NIR and MIR. However, the calculation $\tau_c = 0.1$ fs reproduces much better the general trend even if a constant overestimation is observed all over the spectrum. As reported in works exploring femtosecond excitation dynamics of dielectrics, τ_c is not rigorously a constant and is expected to depend on the free-electron density among other parameters. For instance, simulations on the reflectivity response of sapphire [47] (pulses of 120 fs at 800 nm) reveal a scattering time (inverse of the scattering rate showed on the reference) varying from 1 fs at the beginning of the pulse to values under 0.1 fs from the time at peak intensity for material modification conditions. Accordingly, the relatively good qualitative correspondence obtained with an "averaged" fixed value of 0.1 fs can appear reasonable.

For quantitative analyses, it remains worthwhile to note the significantly different avalanche coefficients derived from our simulations and measurements in comparison to those that can be predicted using the Drude model. While the underlying physical processes behind the determined wavelength dependence of the avalanche coefficient will require more investigations, the obtained data can already serve (with extrapolation) to improve the predictive precision of models based on the standard electron-density rate equation. This holds, for instance, for recent modeling efforts considering a modified electron-density rate equation accounting for the potential influence of ultrafast carrier trapping processes [modified version of Eq. (1)]. The aim of such developments is to assess the expected specificities of the modification response of dielectric materials with the advent of emerging ultrafast MIR laser technologies [50].

C. Crater topography as a function of the wavelength

In previous sections, we concentrate on the measured ablation fluence threshold for the analyses. However, more experimental observables become available above threshold conditions to enrich the discussion on the wavelength dependence of the material responses. In particular, we focus here on the changes of the superficial and volumetric aspects of the produced modifications.

As reported in a previous publication [39] but with a data set limited to two wavelengths (515 and 1550 nm), we confirm here [Fig. 2(a) for $\lambda = 1.7$ μm] that sapphire exhibits always neat craters, without noticeable elevations on the crater borders. In contrast, as can be seen on Fig. 2(a) ($\lambda = 1.7$ μm), soda-lime glass presents notorious elevations at the edges, which has been associated previously to the flow and resolidification of molten material [51]. Those observations, together with similar crater morphologies at different wavelengths, shown within the Supplemental Material [41], confirm that the superficial morphology of the modifications, and therefore the quality of the laser machining depends more on the material characteristics than the applied laser wavelength. Indirectly, this also confirms that the drastic changes of contributions from SFI (MPI or TI) and IMP expected from UV to MIR do not have a clear influence on the processing quality.

Another interesting observable in this context is the obtained crater depths revealing the ability of the different wavelengths to penetrate in the excited transparent materials. This provides both access to more understanding of the physics of interaction and to the ablation efficiency of interest for the potential industrial applications. For clarity of the presentation, we present and discuss here the results obtained on sapphire while also providing similar

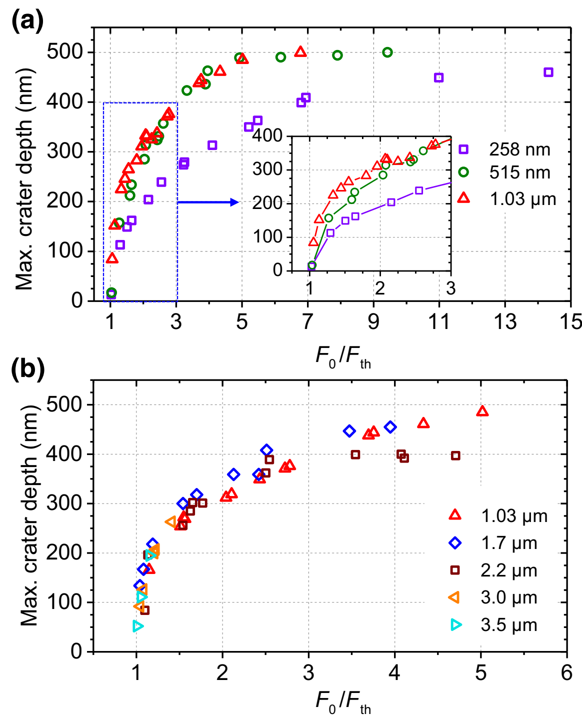

FIG. 8. (a),(b) Maximum crater depth produced sapphire under a single-shot irradiation at different excitation levels (F_0/F_{th}). The inset in (a) shows an enlargement of the data close to the fluence threshold.

data sets for fused silica and soda lime as the Supplemental Material [41].

In Fig. 8, we report the maximum crater depth found in craters (at the center) produced in sapphire as a function of the irradiation peak fluence (F_0). For the ease of comparisons between wavelengths, the x axis is represented normalized with respect to the fluence threshold of ablation (F_0/F_{th}).

A first observation is a systematic saturation behavior on the achievable ablation depth. It is also striking to note a near identical saturation depth for all the considered wavelength at approximately equal to 500 nm here for sapphire (approximately equal to 450 nm for fused silica [41]). Despite the good precision in focus positioning (<10 μm that is significantly smaller than the confocal parameters of all beams), the small differences of the observed plateau levels can be attributed to this question. We make this comment after verifying the sensitivity of this measurement to relative changes of the focusing depth with micrometer precision (Technical Note 2 within the Supplemental Material [41]).

Interestingly, this measured invariance of maximum ablation depth deviates significantly from the predictions of the modeling work of Christensen and Balling [43], where the change of the apparent nonlinearity of interaction by varying the material band gap (3 to 9 eV) or the wavelength in a spectral range much smaller than the one studied here (between 400 and 1060 nm) is leading to more significant variations (deeper machining at longer wavelength). While such experimental quantities are not accessible by our current model, which does not describe pulse propagation into the excited dielectrics, this shows a possibility for improved and more robust simulations by implementing the wavelength-dependent avalanche coefficients derived from our work.

Looking at the details of the ablation depths near threshold conditions, one can note slightly different slopes as a function of the normalized fluence between 1030 and 515 nm and significantly reduced ablation rates at 258 nm [see inset in Fig. 8(a)]. This variation of the energy dependence can be directly attributed to the dominating role of MPI (few photons) expected for UV. This causes a nonlinear Beer-Lambert law that requires more energy increase to see the ablation front penetrating deep inside the matter. Again, given the modest wavelength-dependence of nonlinear absorption in the NIR-MIR domain and the exponential growth of carrier density based on the dominating avalanche mechanism, one can qualitatively understand the more abrupt depth rise before saturation as observed with near invariant measurements in this spectral domain (Fig. 8).

IV. SUMMARY AND CONCLUSIONS

From this work, aiming at a broadband study of single-shot ablation of dielectrics (fused silica, sapphire, and soda lime) with 200-fs pulses, we report on near-invariant responses over a domain ranging from VIS to MIR up to 3.5 μm. This holds for the measured fluence thresholds for ablation and ablation performance (crater morphologies and ablation efficiency) and complements our previous findings on the nonlinearity invariance of machining resolution due to the deterministic threshold nature of ablation in ultrafast regimes [39,40,52].

For fundamental considerations, analyses show a change of dominant photoionization mechanism, from multiphoton to tunneling ionization, when varying the wavelength from VIS to MIR without significant change on the observed ablation performance. We also conclude on a contribution of photoionization to energy deposition in ablation conditions that remain weak over the broadband range of investigated wavelengths. However, multiphoton and tunneling are necessary for seeding the impact ionization mechanism that appears extremely dominant in the whole spectral range (above 99% of the total deposited energy).

For technological considerations, these conclusions open a wide range of possibilities for processing system optimizations with the advent of ultrafast laser technologies emitting in different spectral domains and giving access to different performance advantages. For instance,

one can refer to the kW power level demonstrated with compact fiber laser technologies in the mid-IR (mainly thulium-based fiber lasers) [53]. This can offer solutions for high-throughput production capabilities without compromising machining qualities.

Finally, the only modest variations observed in the UV mean that this spectral domain remains probably the most promising one for accessing even higher processing performances. As shown with a typical twofold decrease of the ablation thresholds, this part of the spectrum is highly favorable for efficient energy coupling to materials, but it is obviously also an optimum in dealing with diffraction limits and thus achieving high-lateral processing resolutions. Interestingly, we also show in this work a more modest sensitivity of machining depth to the applied energy and material for near-threshold conditions (in comparison to VIS-NIR-MIR). This reveals a situation beneficial for reliable material removal with extreme longitudinal resolution. Recently, impressive demonstrations have been made on reliable matter removal with nanometric precision (depth) at the surface of dielectrics materials using NIR femtosecond pulses [54]. On the basis of our findings, even higher precision can be expected using similar pulses (same stability) in the UV domain.

Overall, we believe that this comprehensive report made on the wavelength dependence of ablation is timely considering the increasing diversity of ultrafast laser technologies now emitting in various spectral domains. It is also expected to be beneficial for the development of improved simulations of the complex interaction problem. It specifically helps to better understand the avalanche coefficient, a useful physical parameter in the field of laser processing of materials.

ACKNOWLEDGMENTS

This project has received funding from the European Research Council (ERC) under the European Union's Horizon 2020 research and innovation program (Grant Agreement No. 724480).

TABLE I. Ablation fluence threshold values and its errors on sapphire, UV-fused silica, IR-fused silica, and soda-lime glass. Those values correspond to the ones plotted on Fig. 4(a).

	Fluence threshold of ablation (J cm^{-2})			
λ (nm)	Sapphire	UV-fused silica	IR-fused silica	Soda-lime glass
258	2.4 ± 0.2	2.2 ± 0.4	2.2 ± 0.4	1.1 ± 0.2
515	3.9 ± 0.4	3.1 ± 0.3	3.0 ± 0.3	2.2 ± 0.2
1030	4.2 ± 0.4	3.6 ± 0.4	3.6 ± 0.4	2.6 ± 0.3
1550	4.6 ± 0.5	3.8 ± 0.4	3.8 ± 0.4	3.0 ± 0.3
1700	4.8 ± 0.5	4.2 ± 0.4	4.2 ± 0.4	3.2 ± 0.3
2000	4.9 ± 0.7	4.2 ± 0.6	4.2 ± 0.6	3.2 ± 0.5
2200	4.9 ± 0.5	4.1 ± 0.4	4.3 ± 0.4	—
3000	5.1 ± 0.8	4.3 ± 0.6	—	—
3500	4.7 ± 0.9	4.0 ± 0.8	3.9 ± 0.8	—

APPENDIX A : ABLATION FLUENCE THRESHOLD VALUES OBTAINED IN SAPPHIRE, FUSED SILICA, AND SODA LIME

In Table I are shown the values plotted in Fig. 4. A detailed explanation of the determination criteria of ablation fluence threshold and its errors can be found on a Technical Note in the Supplemental Material [41].

[1] R. R. Gattass and E. Mazur, Femtosecond laser micromachining in transparent materials, Nat. Photonics **2**, 219 (2008).

[2] A. P. Joglekar, H. Liu, E. Meyhöfer, G. Mourou, and A. J. Hunt, Optics at critical intensity: Applications to nanomorphing, Proc. Natl. Acad. Sci. U. S. A. **101**, 5856 (2004).

[3] Z.-Z. Li, L. Wang, H. Fan, Y.-H. Yu, Q.-D. Chen, S. Juodkazis, and H.-B. Sun, O-FIB: Far-field-induced near-field breakdown for direct nanowriting in an atmospheric environment, Light: Sci. Appl. **9**, 41 (2020).

[4] M. F. Yanik, H. Cinar, H. N. Cinar, A. D. Chisholm, Y. Jin, and A. Ben-Yakar, Functional regeneration after laser axotomy, Nature **432**, 822 (2004).

[5] A. Vailionis, E. G. Gamaly, V. Mizeikis, W. Yang, A. V. Rode, and S. Juodkazis, Evidence of superdense aluminium synthesized by ultrafast microexplosion, Nat. Commun. **2**, 1 (2011).

[6] E. Gamaly, *Femtosecond Laser-Matter Interactions Theory, Experiments and Applications* (CRC Press, New York, 2011).

[7] P. Balling and J. Schou, Femtosecond-laser ablation dynamics of dielectrics: Basics and applications for thin films, Rep. Prog. Phys. **76**, 036502 (2013).

[8] M. Garcia-Lechuga, J. Siegel, J. Hernandez-Rueda, and J. Solis, Femtosecond laser ablation of dielectric materials in the optical breakdown regime: Expansion of a transparent shell, Appl. Phys. Lett. **105**, 112902 (2014).

[9] M. Garcia-Lechuga, J. Solis, and J. Siegel, Key stages of material expansion in dielectrics upon femtosecond laser ablation revealed by double-color illumination time-resolved microscopy, Appl. Phys. A **124**, 221 (2018).

[10] M. Malinauskas, A. Žukauskas, S. Hasegawa, Y. Hayasaki, V. Mizeikis, R. Buividas, and S. Juodkazis, Ultrafast Laser Processing of Materials: From Science to Industry, Light: Sci. Appl. **5**, e16133 (2016).

[11] G. Olivié, D. Giguère, F. Vidal, T. Ozaki, J.-C. Kieffer, O. Nada, and I. Brunette, Wavelength dependence of femtosecond laser ablation threshold of corneal stroma, Opt. Express **16**, 4121 (2008).

[12] S. M. Eaton, H. Zhang, P. R. Herman, F. Yoshino, L. Shah, J. Bovatsek, and A. Y. Arai, Heat accumulation effects in femtosecond laser-written waveguides with variable repetition rate, Opt. Express **13**, 4708 (2005).

[13] C. Kerse, Hamit Kalaycıoğlu, Parviz Elahi, Barbaros Çetin, Denizhan K. Kesim, Önder Akçaalan, Seydi Yavaş,

Mehmet D. Aşık, Bülent Öktem, Heinar Hoogland, Ronald Holzwarth and Fatih Ömer Ilday, Ablation-cooled material removal with ultrafast bursts of pulses, Nature **537**, 84 (2016).

[14] P. P. Rajeev, M. Gertsvolf, P. B. Corkum, and D. M. Rayner, Field Dependent Avalanche Ionization Rates in Dielectrics, Phys. Rev. Lett. **102**, 083001 (2009).

[15] M. Lebugle, N. Sanner, N. Varkentina, M. Sentis, and O. Utéza, Dynamics of femtosecond laser absorption of fused silica in the ablation regime, J. Appl. Phys. **116**, 063105 (2014).

[16] A. C. Tien, S. Backus, H. Kapteyn, M. Murnane, and G. Mourou, Short-Pulse Laser Damage in Transparent Materials as a Function of Pulse Duration, Phys. Rev. Lett. **82**, 3883 (1999).

[17] V. Temnov, K. Sokolowski-Tinten, P. Zhou, A. El-Khamhawy, and D. von der Linde, Multiphoton Ionization in Dielectrics: Comparison of Circular and Linear Polarization, Phys. Rev. Lett. **97**, 237403 (2006).

[18] D. Giguère, G. Olivié, F. Vidal, S. Toetsch, G. Girard, T. Ozaki, J.-C. Kieffer, O. Nada, and I. Brunette, Laser ablation threshold dependence on pulse duration for fused silica and corneal tissues: Experiments and modeling, J. Opt. Soc. Am. A **24**, 1562 (2007).

[19] B. Chimier, O. Utéza, N. Sanner, M. Sentis, T. Itina, P. Lassonde, F. Légaré, F. Vidal, and J. C. Kieffer, Damage and ablation thresholds of fused-silica in femtosecond regime, Phys. Rev. B **84**, 094104 (2011).

[20] O. Utéza, N. Sanner, B. Chimier, A. Brocas, N. Varkentina, M. Sentis, P. Lassonde, F. Légaré, and J. C. Kieffer, Control of material removal of fused silica with single pulses of few optical cycles to sub-picosecond duration, Appl. Phys. A **105**, 131 (2011).

[21] L. V. Keldysh, Ionization in the field of a strong electromagnetic wave, Sov. Phys. JETP **20**, 1307 (1965).

[22] L. V. Keldysh, Concerning the theory of impact ionization in semiconductors, Sov. Phys. JETP **21**, 1135 (1965).

[23] D. M. Simanovskii, H. A. Schwettman, H. Lee, and A. J. Welch, Midinfrared Optical Breakdown in Transparent Dielectrics, Phys. Rev. Lett. **91**, 107601 (2003).

[24] T. Q. Jia, H. X. Chen, M. Huang, F. L. Zhao, X. X. Li, S. Z. Xu, H. Y. Sun, D. H. Feng, C. B. Li, X. F. Wang, R. X. Li, Z. Z. Xu, X. K. He, and H. Kuroda, Ultraviolet-infrared femtosecond laser-induced damage in fused silica and CaF_2 crystals, Phys. Rev. B **73**, 054105 (2006).

[25] D. Grojo, S. Leyder, P. Delaporte, W. Marine, M. Sentis, and O. Utéza, Long-wavelength multiphoton ionization inside band-gap solids, Phys. Rev. B **88**, 195135 (2013).

[26] L. Gallais, D.-B. Douti, M. Commandré, G. Batavičiūtė, E. Pupka, M. Ščiuka, L. Smalakys, V. Sirutkaitis, and A. Melninkaitis, Wavelength dependence of femtosecond laser-induced damage threshold of optical materials, J. Appl. Phys. **117**, 223103 (2015).

[27] E. Migal, E. Mareev, E. Smetanina, G. Duchateau, and F. Potemkin, Role of wavelength in photocarrier absorption and plasma formation threshold under excitation of dielectrics by high-intensity laser field tunable from visible to mid-IR, Sci. Rep. **10**, 1 (2020).

[28] D. R. Austin, K. R. P. Kafka, Y. H. Lai, Z. Wang, C. I. Blaga, and E. A. Chowdhury, Femtosecond laser damage of germanium from near- to mid-infrared wavelengths, Opt. Lett. **43**, 3702 (2018).

[29] J. Hernandez-Rueda, J. Clarijs, D. Van Oosten, and D. M. Krol, the influence of femtosecond laser wavelength on waveguide fabrication inside fused silica, Appl. Phys. Lett. **110**, 161109 (2017).

[30] M. Chambonneau, L. Lavoute, D. Gaponov, V. Y. Fedorov, A. Hideur, S. Février, S. Tzortzakis, O. Utéza, and D. Grojo, Competing Nonlinear Delocalization of Light for Laser Inscription Inside Silicon with a 2-μm Picosecond Laser, Phys. Rev. Appl. **12**, 024009 (2019).

[31] M. Garcia-Lechuga, N. Casquero, A. Wang, D. Grojo, and J. Siegel, Deep silicon amorphization induced by femtosecond laser pulses up to the mid-infrared, Adv. Opt. Mater. **9**, 2100400 (2021).

[32] T. Otobe, Wavelength Dependence of the Laser-Excitation Process on a Silicon Surface, Phys. Rev. Appl. **13**, 024062 (2020).

[33] N. Linz, S. Freidank, X. X. Liang, and A. Vogel, Wavelength dependence of femtosecond laser-induced breakdown in water and implications for laser surgery, Phys. Rev. B **94**, 024113 (2016).

[34] M. Garcia-Lechuga and D. Grojo, Simple and robust method for determination of laser fluence thresholds for material modifications: an extension of Liu's approach to imperfect beams, Open Res. Eur. **1**, 7 (2021).

[35] L. Gallais and M. Commandré, Laser-induced damage thresholds of bulk and coating optical materials at 1030 nm, 500 fs, Appl. Opt. **53**, A186 (2013).

[36] N. M. Ravindra and J. Narayan, Optical properties of amorphous silicon and silicon dioxide, J. Appl. Phys. **60**, 1139 (1986).

[37] G.-L. Tan, M. F. Lemon, and R. H. French, Optical properties and london dispersion forces of amorphous silica determined by vacuum ultraviolet spectroscopy and spectroscopic ellipsometry, J. Am. Ceram. Soc. **86**, 1885 (2003).

[38] R. H. French, Electronic band structure of Al_2O_3, with comparison to Alon and AIN, J. Am. Ceram. Soc. **73**, 477 (1990).

[39] M. Garcia-Lechuga, O. Utéza, N. Sanner, and D. Grojo, Evidencing the nonlinearity independence of resolution in femtosecond laser ablation, Opt. Lett. **45**, 952 (2020).

[40] M. Garcia-Lechuga, G. Gebrayel El Reaidy, H. Ning, P. Delaporte, and D. Grojo, Assessing the limits of determinism and precision in ultrafast laser ablation, Appl. Phys. Lett. **117**, 171604 (2020).

[41] See Supplemental Material at http://link.aps.org/supplemental/10.1103/PhysRevApplied.19.044047 showing crater morphologies, maximum crater depths on fused silica and soda lime and two Technical Notes.

[42] J. M. Liu, Simple technique for measurements of pulsed Gaussian-beam spot sizes, Opt. Lett. **7**, 196 (1982).

[43] B. Christensen and P. Balling, Modeling ultrashort-pulse laser ablation of dielectric materials, Phys. Rev. B **79**, 155424 (2009).

[44] C. Quoix, G. Hamoniaux, A. Antonetti, J.-C. Gauthier, J.-P. Geindre, and P. Audebert, Ultrafast plasma studies by phase and amplitude measurements with femtosecond spectral interferometry, J. Quant. Spectrosc. Radiat. Transfer **65**, 455 (2000).

[45] E. G. Gamaly and A. V. Rode, Transient optical properties of dielectrics and semiconductors excited by an ultrashort laser pulse, J. Opt. Soc. Am. B **31**, C36 (2014).

[46] D. Puerto, J. Siegel, W. Gawelda, M. Galvan-Sosa, L. Ehrentraut, J. Bonse, and J. Solis, Dynamics of plasma formation, relaxation, and topography modification induced by femtosecond laser pulses in crystalline and amorphous dielectrics, J. Opt. Soc. Am. B **27**, 1065 (2010).

[47] M. Garcia-Lechuga, L. Haahr-Lillevang, J. Siegel, P. Balling, S. Guizard, and J. Solis, Simultaneous time-space resolved reflectivity and interferometric measurements of dielectrics excited with femtosecond laser pulses, Phys. Rev. B **95**, 214114 (2017).

[48] M. Grehn, T. Seuthe, M. Höfner, N. Griga, C. Theiss, A. Mermillod-Blondin, M. Eberstein, H. Eichler, and J. Bonse, Femtosecond-laser induced ablation of silicate glasses and the intrinsic dissociation energy, Opt. Mater. Express **4**, 689 (2014).

[49] I. H. Malitson, Interspecimen comparison of the refractive index of fused silica, J. Opt. Soc. Am. **55**, 1205 (1965).

[50] G. D. Tsibidis and E. Stratakis, Ionization dynamics and damage conditions in fused silica irradiated with mid-infrared femtosecond pulses, Appl. Phys. Lett. **122**, 043501 (2023).

[51] A. Ben-Yakar, R. L. Byer, A. Harkin, J. Ashmore, H. A. Stone, M. Shen, and E. Mazur, Morphology of femtosecond-laser-ablated borosilicate glass surfaces, Appl. Phys. Lett. **83**, 3030 (2003).

[52] P. Sopeña, M. Garcia-Lechuga, A. Wang, and D. Grojo, Ultrafast laser stabilization by nonlinear absorption for enhanced-precision material processing, Opt. Lett. **47**, 993 (2022).

[53] C. Gaida, M. Gebhardt, T. Heuermann, F. Stutzki, C. Jauregui, and J. Limpert, Ultrafast thulium fiber laser system emitting more than 1 kW of average power, Opt. Lett. **43**, 5853 (2018).

[54] G. Chen and J. Qiao, Femtosecond-laser-enabled simultaneous figuring and finishing of glass with a subnanometer optical surface, Opt. Lett. **47**, 3860 (2022).

[55] C. Pasquier, M. Sentis, O. Utéza, and N. Sanner, Predictable surface ablation of dielectrics with few-cycle laser pulse even beyond air ionization, Appl. Phys. Lett. **109**, 051102 (2016).